SCIENCE CHINA Materials

ARTICLES

mater.scichina.com link.springer.com

Published online 18 September 2015 | doi: 10.1007/s40843-015-0082-x
Sci China Mater 2015, 58: 683–692

α- and γ-Fe_2O_3 nanoparticle/nitrogen doped carbon nanotube catalysts for high-performance oxygen reduction reaction

Meng Sun[1,2], Gong Zhang[1,2], Huijuan Liu[1], Yang Liu[3] and Jinghong Li[3*]

Developing transition metal oxides/carbon substrate hybrids as highly promising non-precious metal oxygen reduction reaction (ORR) electrocatalysts is crucial to replace the scarce platinum and solve the world-wide energy predicament. In this work, γ-Fe_2O_3/N-carbon nanotubes (N-CNTs) and α-Fe_2O_3/N-CNTs nanocatalysts were successfully synthesized by simultaneous formation of crystal configuration of Fe_2O_3 and the doping of nitrogen on CNTs. α-Fe_2O_3/N-CNTs catalysts exhibited superior ORR electrocatalytic activity with lower onset and peak potential of −0.21 and −0.27 V, and possessed a more efficient four-electron-dominant ORR process compared with γ-Fe_2O_3/N-CNTs, N-CNTs and CNTs. The crystal distortions on octahedral α-Fe_2O_3 held great potential for displacement of either iron or other ions, serving as the active sites and contributing to its better ORR catalytic ability than the vacancies integrated in γ-Fe_2O_3/N-CNTs. Both the two nanocatalysts possessed superior methanol tolerance and long-term stability of ORR compared with Pt/C, indicating great potential for their practical utilization in fuel cells.

INTRODUCTION

The cathodic oxygen reduction reaction (ORR) is of great promise in solving the worldwide energy crisis in the near future. With the rapid development of the various research fields related with ORR, the ongoing improvement of ORR for these applications is greatly demanded [1–3]. How to simultaneously minimize the ORR procedure of a two-electron transfer with the production of H_2O_2 as the intermediate, while maximize an efficient four-electron process to generate H_2O as the end product, is essential for the promotion of the sluggish ORR kinetics. Although noble metal-based electrocatalysts (e.g., Pt/C) have largely elevated the efficiency of electron transfer via an ideal ORR process, the crossover effects, CO poisoning, unsatisfactory stability and high cost still restricted their large-scale industrialization [4]. Therefore, exploring cost-effective no-noble metal ORR electrocatalyst to overcome aforesaid problems is still in full of challenge.

α-Fe_2O_3, as the principal component in earth-abundant hematite, is the most stable ferric oxide and famous n-type semiconductor with favorable band gap and valence band edge position [5]. In a typical α-Fe_2O_3 crystal, the slight distortions exposing from the Fe^{3+}-filled octahedra construction can cause regular displacement of either Fe ions or other metallic ions, serving as the active sites, greatly contributing to the excellent catalytic ability. Thanks to the inherent advantage, it has been widely studied for gas sensor [6], photo/electrocatalyst [7–9], and lithium-ion battery [10] in recent years. γ-Fe_2O_3 is another special crystal system of Fe_2O_3 with cubic or tetragonal structure occupying amounts of interstices, in which 5/6 of these positions are only occupied by Fe^{3+}, remaining about 1/6 are vacancies [11]. The vacancies hold great potential in accelerating electron transfer efficiency and increasing promising active sites for catalytic reaction [12]. Therefore, the γ-Fe_2O_3 also exhibits perfect performance in a variety of applications [13–15]. Although sorts of strategies such as morphology tailoring [16], multi-dimensionality assembly [17], heterojunction composition [18], and impurity doping [19] have been successfully applied to promote their catalytic activity for further expeditions, there is no remarkable progress on the electrocatalytic ORR.

The nitrogen doped carbon nanotubes (N-CNTs) [20], as an ideal carbonaceous support, have been widely proved to modify the electronic properties of the sp^2-hybridized carbon matrix. The generated surface defects by mass nitrogen chemical doping intrinsically break the balance of

[1] Key Laboratory of Drinking Water Science and Technology, Research Center for Eco-Environmental Sciences, Chinese Academy of Sciences, Beijing 100085, China
[2] University of Chinese Academy of Sciences, Beijing 100039, China
[3] Department of Chemistry, Beijing Key Laboratory for Microanalytical Methods and Instrumentation, Tsinghua University, Beijing 100084, China
[*] Corresponding author (email: jhli@mail.tsinghua.edu.cn)

electron distribution, becoming countless ORR active sites [21]. Undoubtedly, the N-CNTs are qualified as more favorable substrates for the anchoring of Fe_2O_3 for catalytic ORR. This assembly structure can avoid the defects on weak conductivity and agglomeration of Fe_2O_3 particles during electrochemical process. More importantly, it exerts superiorities of the self-construction, resulting in an optimal exposure of activate sites and electron holes for ORR. In this sense, it is wise to take N-CNTs as the support to synthesize γ-Fe_2O_3 or α-Fe_2O_3/N-CNTs hybrids for effective ORR, which reveal the different ORR performance deriving from the different crystal structure Fe_2O_3/N-CNTs.

Herein, γ-Fe_2O_3/N-CNTs and α-Fe_2O_3/N-CNTs were synthesized by following a two-step synthesis method modified from our previous work [8]. Firstly, the precursor of iron-contained grain coated CNTs nanocomposite was heated at 140°C in the air to form ferric oxides/CNTs. These intermediates were further treated by calcination in nitrogen/ammonia atmosphere at 450 and 650°C, respectively. During nitrogen annealing, the formation of different crystals of Fe_2O_3 and the doping of nitrogen on CNTs were respectively accomplished. X-ray diffraction (XRD), scanning electron microscopy (SEM), transmission electron microscopy (TEM), X-ray photoelectron spectroscopy (XPS) and Raman spectroscopy were employed to characterize the γ-Fe_2O_3/N-CNTs and α-Fe_2O_3/N-CNTs. The results indicated that the well-defined γ-Fe_2O_3 nanotubes and α-Fe_2O_3 nanospheres were well supported on the surface of N-CNTs with nitrogen loading of less than 2%. In comparison, α-Fe_2O_3/N-CNTs nanocomposites exhibit better catalytic performance for ORR with a predominantly four-electron transfer pathway than that of γ-Fe_2O_3/N-CNTs, N-CNTs and CNTs. The superb methanol tolerance and long-term catalytic stability of the two nanocomposites compare favorably to those of commercial Pt/C in alkaline condition, indicating great promise for their practical utilization in fuel cells.

EXPERIMENTAL SECTION

Materials

$FeCl_3{\cdot}6H_2O$, HCl, H_2SO_4, $K_4[Fe(CN)_6]$, $K_3[Fe(CN)_6]$, KCl and KOH were obtained from Sinopharm Chemical Reagent Co., Ltd. (Shanghai, China). Nafion stock solution (5 wt.%, Dupont) was supplied by Alfa Aesar. CNTs (99.99%, 325 mesh) were obtained from Tsinghua University (Beijing, China). Ultrapure water used in this experiment was generated by a Millipore Water Purification System (Advantage 10, Millipore) with a resistivity of ⩾ 18.2 MΩ cm. All reagents were analytically pure and used as received.

Synthesis of N-CNTs, γ-Fe_2O_3/N-CNTs and α-Fe_2O_3/N-CNTs

The activation process of pristine CNTs by nitric acid (HNO_3, 68 wt.%) was followed by the reported literature and prepared for further utilization [22]. The N-CNTs were synthesized by an annealing method [23], in which the activated CNTs were heated at 800°C with a rate of 5°C min^{-1} in N_2/NH_3 (v/v = 2:1) gas and held for 3 h. The resulting black products were washed by ultrapure water and ethanol for three times. For the synthesis of the two different crystal ferric oxides supported N-doped CNTs nanocatalysts [8,24], 100 mg of activated CNTs were stirred at 600 rpm in ethanol-water (v/v = 5%) solution at room temperature for 1 h, followed by 10 min of ultrasonic treatment. Subsequently, 0.35 mL fresh 0.1 mol L^{-1} aqueous $FeCl_3{\cdot}6H_2O$ was added quickly and the solvent was dried at 60°C for 12 h. Finally, the dried composites were gradually heated to 140°C in air and kept for 8 h, then heated to 450°C in N_2/NH_3 (v/v = 2:1) gas with 2°C min^{-1} and held for 3 h, resulting in the products of α-Fe_2O_3/N-CNTs; as it was heated to 650°C in the same N_2/NH_3 condition with 2°C min^{-1} and held for 3 h, γ-Fe_2O_3/N-CNTs were thus synthesized.

Characterization

The crystal structure was determined using XRD measurements (Bruker D8 Advance) between 10° and 80° at a scan step of 20° min^{-1} operating at 40 kV and 30 mA using Cu Ka radiation. TEM and high-resolution TEM (HRTEM) images were obtained with a TEM H-800 (Hitachi, Japan) at an accelerating voltage of 220 kV. Energy-dispersive X-ray spectrum (EDS) was analyzed by an energy dispersive spectroscopy analyser attached to the HRTEM. The XPS data was performed with an AXIS-Ultra instrument (Kratos Analytical, UK) using monochromatic Al Ka radiation (225 W, 15 mA, 15 kV). Binding energies were standardized with the C 1s line at 284.80 eV. Raman spectra were recorded on a microscopic confocal Raman spectrometer (JY Lab Raman HR 800) with an excitation laser source of 785 nm.

Electrochemical measurements

The conventional three-electrode system was assembled with an as-synthesized nanocatalyst-coated glassy carbon electrode (GCE), an Ag|AgCl/KCl (saturated) reference electrode and Pt wire as a counter electrode. The GCE should be polished by using 0.3 mm aluminium oxide slurry and washed with ethanol and ultrapure water in sequence in an ultrasonic bath before being used. Catalyst ink was obtained by mixing solid catalyst (2 mg) with Nafion solution (1 mL) under sufficient sonication for 30 min. Finally, 6 and 20 mL of the prepared inks were dropped onto the

prepared GCE with diameters of 3 mm for cyclic voltammetry (CV) test, and 5 mm for rotating-disk electrode (RDE) measurement, respectively. Electrochemical measurements were performed using a CHI 830 electrochemical analyzer coupled with an RDE system (Princeton Applied Research, Model 616). Additionally, the electrochemical impedance spectroscopy (EIS) tests were operated by applying an AC voltage of 10 mV amplitude with frequency from 100 Hz to 100 kHz in 5 mmol L^{-1} $K_3[Fe(CN)_6]/K_4[Fe(CN)_6]$ (1:1) redox probe solution. All the experiments were conducted at room temperature.

RESULTS AND DISCUSSION

Fig. 1a shows the powder XRD patterns of γ-Fe_2O_3/N-CNTs, α-Fe_2O_3/N-CNTs, N-CNTs and CNTs. The N-CNTs exhibited two typical carbon peaks located at 25° and 43°, both of which just expanded the peak width slightly compared to CNTs. The distinct strong diffraction peaks can be observed corresponding to the (220), (311), (400), (422), (511) and (440) peaks from γ-Fe_2O_3/N-CNTs, which precisely matched those of pure γ-Fe_2O_3 crystals (JCPDS card No. 39-1346), indicating that the γ-Fe_2O_3 with good crystallinity successfully grew on the N-CNTs. Similarly, the XRD pattern of α-Fe_2O_3/N-CNTs was also well identical to that of standard α-Fe_2O_3 (JCPDS card No. 33-0664). Further confirmation of the structural information of nitrogen-doping (N-doping) on CNTs was obtained from the Raman spectra (Fig. 1b). The characteristic D and G peaks in the wavenumber located at around 1356 and 1609 cm^{-1}, respectively. Generally, the change of I_D/I_G value offers strong evidence of the reduction degree and N-doping in CNTs, in which D peaks suggest the degree of defects and G peaks always indicate the in-plane stretching vibration of carbon atom sp^2 hybridization [25]. The I_D/I_G ratio of 1.12 in N-CNTs indicates a lower crystallinity and higher degree of N-doping than that of 1.04 in CNTs. In comparison, for γ-Fe_2O_3/N-CNTs and α-Fe_2O_3/N-CNTs, the obtained I_D/I_G value of α-Fe_2O_3/N-CNTs was 1.26, higher than that of γ-Fe_2O_3/N-CNTs (1.18), revealing that the growth of different crystal structure of Fe_2O_3 significantly enhanced the heteroatom doping on CNTs. Obviously, with the same weight load of iron, the prepared α-Fe_2O_3/N-CNTs resulted in more defects of N-doping compared with γ-Fe_2O_3/N-CNTs, which might influence their ORR performance to some extent.

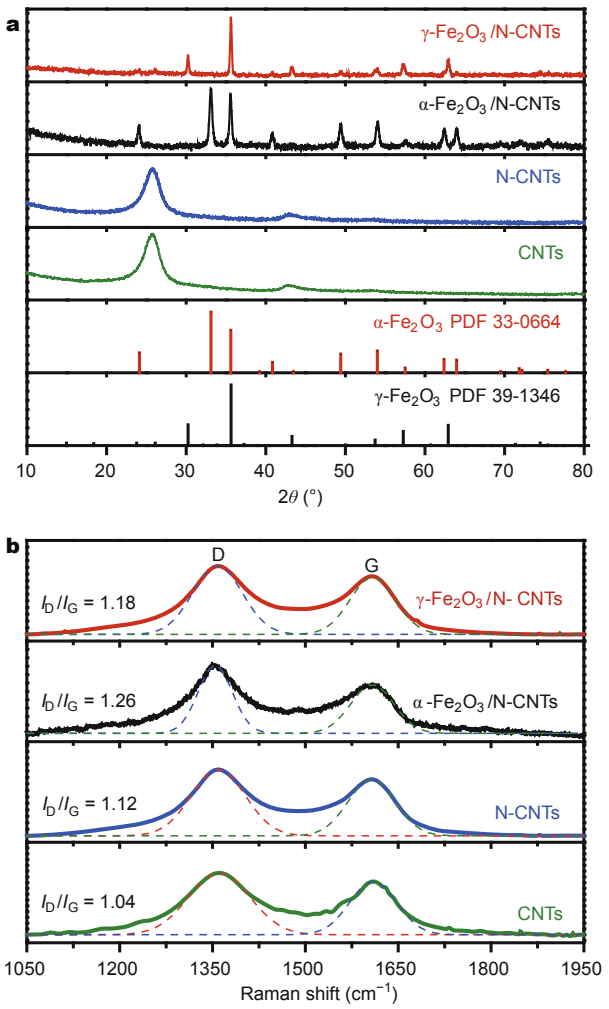

Figure 1 (a) XRD patterns of the γ-Fe_2O_3/N-CNTs, α-Fe_2O_3/N-CNTs, N-CNTs and CNTs. (b) Raman spectra of typical carbon regions of γ-Fe_2O_3/N-CNTs, α-Fe_2O_3/N-CNTs, N-CNTs and CNTs.

XPS is a powerful tool to identify the elemental states in bulk nanoscale γ-Fe_2O_3/N-CNTs and α-Fe_2O_3/N-CNTs. As shown in Fig. 2a, both the two nanocatalysts show the peaks at around 710, 719 and 724 eV, representing the binding energies of Fe $2p_{3/2}$, shake-up satellite Fe $2p_{3/2}$, and Fe $2p_{1/2}$ of Fe^{3+}, suggesting the excellent formation of pure Fe_2O_3 without impurities [8]. Particularly, the only signals on γ-Fe_2O_3/N-CNTs were observed expressly for Fe^{2+} at 59.2 eV of Fe 3p and at 79.2 eV of Fe 3s, explaining the specific structural characteristics of cubic γ-Fe_2O_3 with Fe^{2+} occupied vacancies. Furthermore, the high-resolution XPS spectra of N 1s, C 1s and O 1s provided more information in confirming the nature of the binding among oxygen, carbon and nitrogen in detail. As shown in Fig. 2b, the N 1s peaks were both observed at 399.9 eV for pyrrolic-N and 401.5 eV for quaternary-N [26,27] from γ-Fe_2O_3/N-CNTs, and corresponding binding energy (BE) at 399.7 eV and 401.7 eV from α-Fe_2O_3/N-CNTs, indicating that the heteroatom nitrogen successfully doped on the CNTs. Compared with the γ-Fe_2O_3/N-CNTs, α-Fe_2O_3/N-CNTs held a decreasing baseline noise and increasing peak intensity of

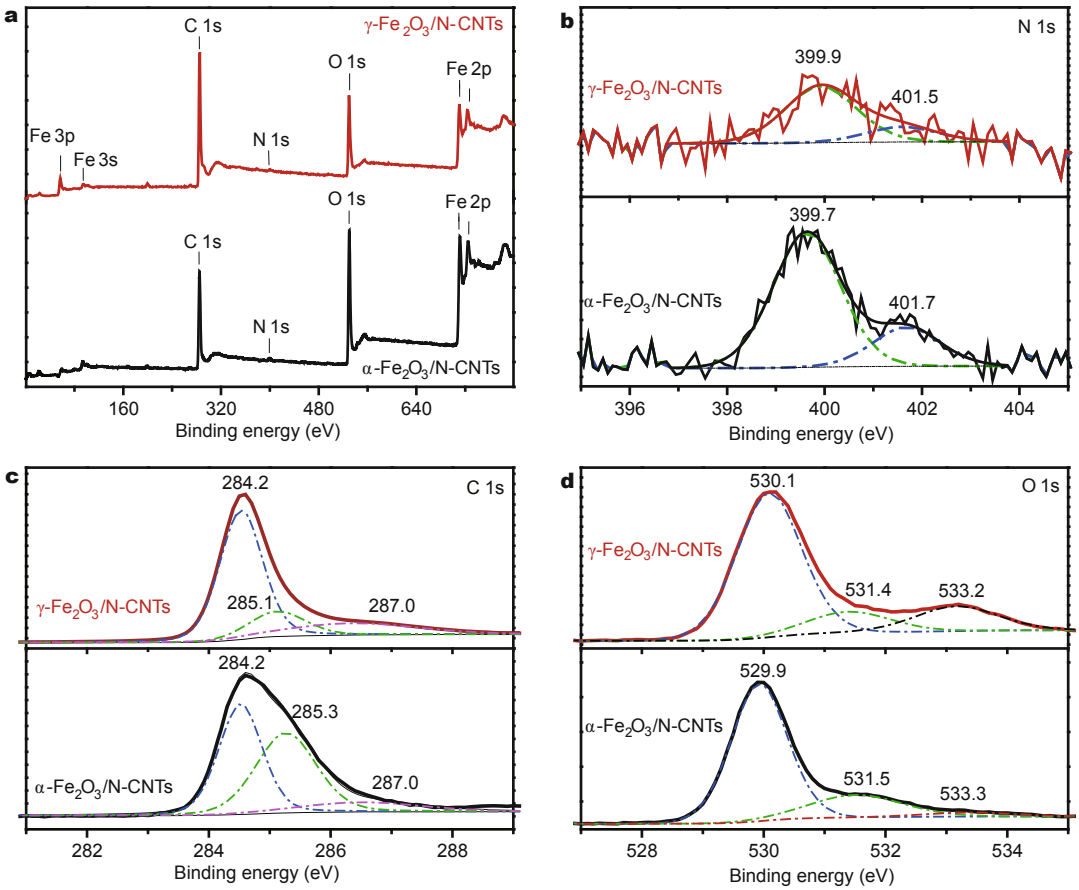

Figure 2 (a) XPS survey spectra of the full scan of γ-Fe_2O_3/N-CNTs and α-Fe_2O_3/N-CNTs. High-resolution XPS spectrum of (b) N 1s, (c) C 1s, (d) O 1s regions of the γ-Fe_2O_3/N-CNTs and α-Fe_2O_3/N-CNTs.

quaternary-N, which further demonstrates an enhanced level of N-doping on α-Fe_2O_3/N-CNTs. Table 1 lists the atomic content of carbon, nitrogen, oxygen and iron of γ-Fe_2O_3/N-CNTs and α-Fe_2O_3/N-CNTs obtained from XPS and EDS results, respectively. Thermal treatment in N_2/NH_3 condition introduced an average of 1.06% N into γ-Fe_2O_3/N-CNTs. While under the same amount of iron precursor, the formation of α-Fe_2O_3/N-CNTs increased N percentage up to mean 1.94%. Fig. 2c shows the typical C 1s peak ranging from 282 to 290 eV, around which there are three different C bonds in the chemically modified CNTs: C–C at 284.2 eV, C–OH at around 285.3 eV, and C=O at 287.0 eV. It is well-known that the peak of C=O is often overlaid with C–N around the binding energy of 287.5 ± 0.5 eV [28]. Therefore, the peak at 287.0 eV for C=O or C–N on α-Fe_2O_3/N-CNTs increased slightly to γ-Fe_2O_3/N-CNTs, further providing the evidence of an intensive doping of nitrogen in α-Fe_2O_3/N-CNTs. Additionally, the apparent increase of C–OH peak at around 285.3 eV on α-Fe_2O_3/N-CNTs suggests that it possesses more oxygen-contained active sites on the surface of N-CNTs than that of γ-Fe_2O_3/N-CNTs. These sites supply not only sufficient and potential

Table 1 Atomic composition of C, O, N, and Fe of the synthesized γ-Fe_2O_3/N-CNTs and α-Fe_2O_3/N-CNTs

Sample	C (%)	N (%)	O (%)	Fe (%)	Data source
γ-Fe_2O_3/N-CNTs	87.68	1.02	6.98	4.32	XPS
	86.42	1.10	7.91	4.57	EDS
α-Fe_2O_3/N-CNTs	86.85	1.85	7.52	3.78	XPS
	87.50	2.03	7.16	3.31	EDS

locations for the N-doping, but also create convenience in surface functionalization for α-Fe_2O_3/N-CNTs to develop the electrocatalytic ORR activity further. Similarly, the advantage of the O 1s peaks at 531.5 eV on α-Fe_2O_3/N-CNTs mainly fits the signals of oxygen bridge (–O–) on the interfaces of N-CNTs, revealing its capacity in combining active addends as well (Fig. 2d).

To reveal the morphologies and microscopic structures, the synthesized γ-Fe_2O_3/N-CNTs and α-Fe_2O_3/N-CNTs were characterized by TEM and HRTEM. As shown in Fig. 3a, the cubic γ-Fe_2O_3 being spiral growth along the different axis centers is stably distributed on the compact three-dimensional (3D) spaces formed by the stacked CNTs. The interlaced CNTs are highly interconnected, providing stable spaces for the formation and dispersion of Fe_2O_3 nanoparticles, and also enhancing the multidimensional electron transfer pathways. The corresponding HRTEM image (Fig. 3b) demonstrates that a well-defined crystalline lattice can be observed with a spacing of 2.51 Å, matching with the mainly exposed (311) face of γ-Fe_2O_3 nanocrystal. The inset of Fig. 3b illustrates its deductive schematic drawings of the exposed (311) faces of cubic γ-Fe_2O_3 according to the HRTEM. In Fig. 3c, the as-synthesized α-Fe_2O_3 shaped like an ellipsoid with the approximate size of 100 nm scattering on the CNT surface can be clearly seen. The inset in Fig. 3c shows the parallel results of component of iron, carbon, nitrogen and oxygen in α-Fe_2O_3/N-CNTs. While, as a result of thermal processing of ferric oxide to 650°C in N_2/NH_3, the dominant face of α-Fe_2O_3 has been changed to (104) with an exact measured lattice of 2.69 Å (see Fig. 3d).

The cyclic voltammograms (CVs) of ORR on the γ-Fe_2O_3/N-CNTs, α-Fe_2O_3/N-CNTs, N-CNTs and CNTs in O_2-saturated 0.1 mol L^{-1} KOH solutions are shown in Fig. 4a. Obviously, the N-CNTs exhibited more pleasurable ORR performance with lower peak potential of −0.36 V than that of −0.44 V on CNTs alone, confirming the superiority of nitrogen doped ORR reaction site. However, it possessed relatively poorer ORR catalytic activity compared with γ-Fe_2O_3/N-CNTs and α-Fe_2O_3/N-CNTs owing to its onset and reduction peak potential at around −0.28 and −0.35 V, respectively. The results indicated that the introduction of ferric oxide accelerated the electron transfer pathways and contributed to electroactive ORR sites. Compared with γ-Fe_2O_3/N-CNTs and α-Fe_2O_3/N-CNTs, although γ-Fe_2O_3/N-CNTs show similar cathodic peak current to α-Fe_2O_3/N-CNTs, it has a more negative onset

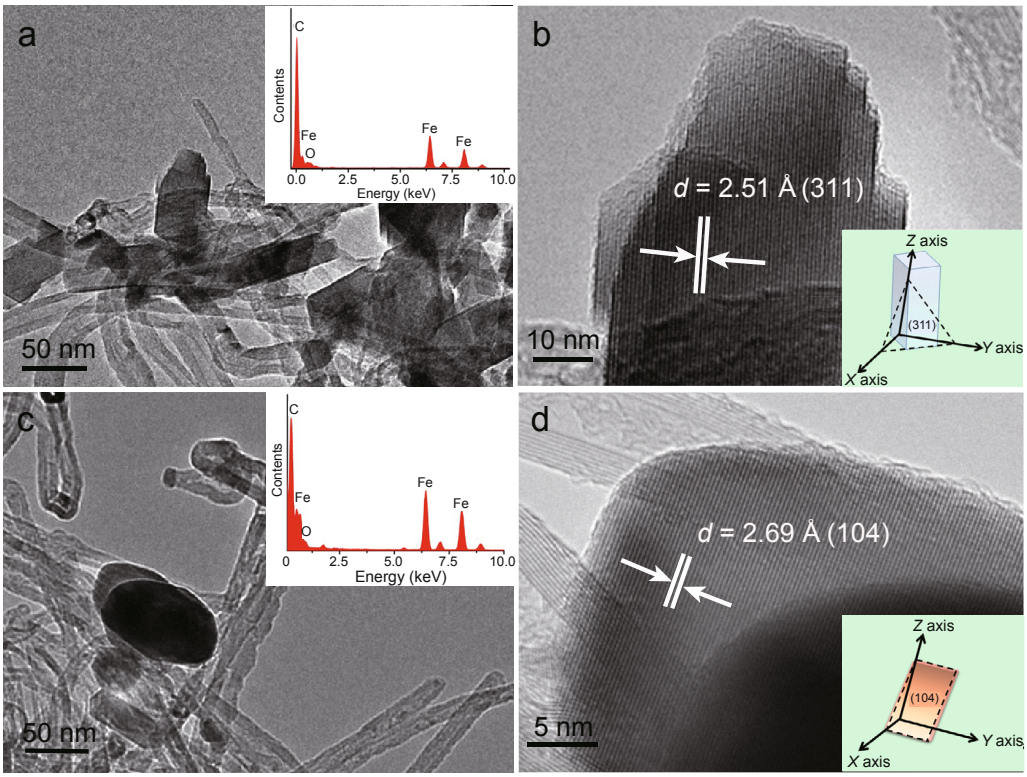

Figure 3 (a) TEM and (b) HRTEM images of γ-Fe_2O_3/N-CNTs; (c) TEM and (d) HRTEM images of α-Fe_2O_3/N-CNTs. The insets of (a) and (c) show the corresponding EDS patterns and the insets of (b) and (d) show the corresponding schematic drawings of the exposed crystal faces.

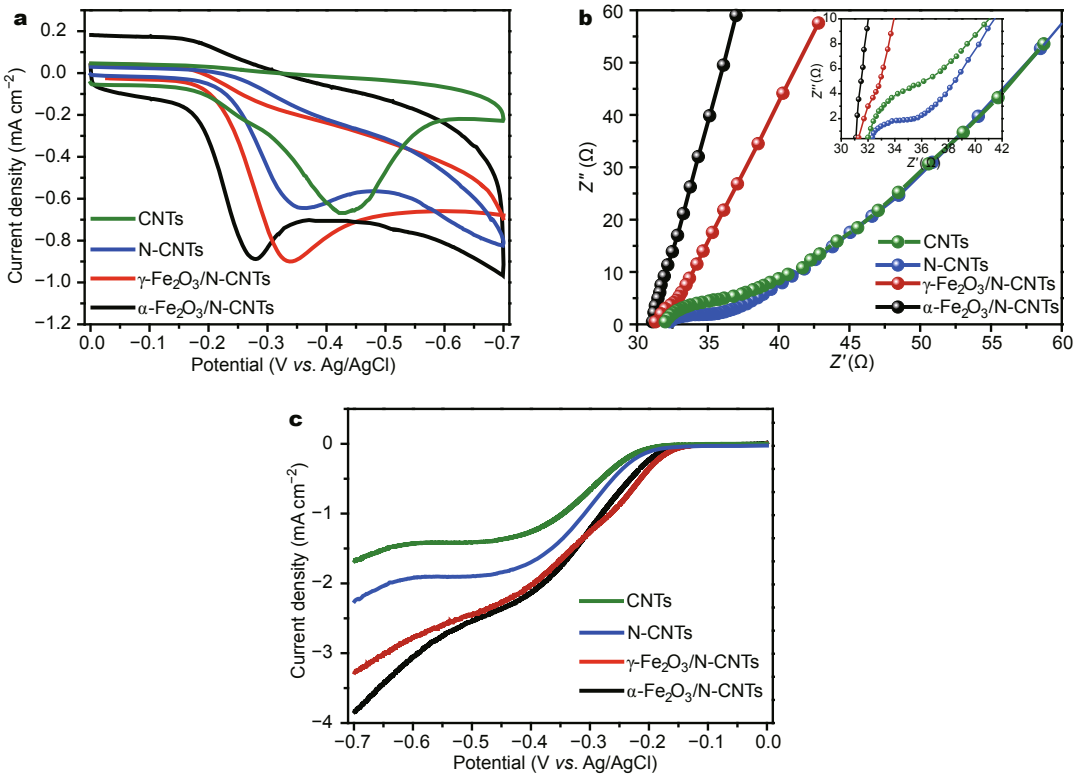

Figure 4 (a) CV curves of the γ-Fe_2O_3/N-CNTs, α-Fe_2O_3/N-CNTs, N-CNTs and CNTs in O_2-saturated 0.1 mol L^{-1} KOH solution. Scan rate: 50 mV s^{-1}. (b) EIS of the γ-Fe_2O_3/N-CNTs, α-Fe_2O_3/N-CNTs, N-CNTs and CNTs in 5 mmol L^{-1} $Fe(CN)_6^{3-/4-}$ containing 0.5 mol L^{-1} KCl solution. The frequency range is from 60 mHz to 60 kHz with signal amplitude of 10 mV. The inset shows the corresponding Nyquist plots in low-frequency region. (c) LSV curves of γ-Fe_2O_3/N-CNTs, α-Fe_2O_3/N-CNTs, N-CNTs and CNTs in O_2-saturated 0.1 mol L^{-1} KOH solution at a rotation rate of 1600 rpm. Sweep rate: 5 mV s^{-1}.

potential at −0.25 V and peak potential at −0.33 V than α-Fe_2O_3/N-CNTs with the onset potential at −0.21 V and peak potential at −0.27 V, respectively. These results indicated that α-Fe_2O_3/N-CNTs owned a remarkable improvement of ORR property to γ-Fe_2O_3/N-CNTs. This promotion of ORR activity was highly depended on the crystal configuration of α-Fe_2O_3, and greatly benefited from the superior mounts of N-doped sites introduced by α-Fe_2O_3, but not γ-Fe_2O_3.

The electron transfer ability of nanocatalysts was also investigated by EIS. As shown in Fig. 4b, the characteristic impedance curves (Nyquist plots) of CNTs, N-CNTs, γ-Fe_2O_3/N-CNTs and α-Fe_2O_3/N-CNTs electrodes with the decreasing diameters of the semicircles in sequence are clearly observed. Obviously, the CNTs coated GCE possessed largest diameter of the semicircle in low-frequency region than N-CNTs, γ-Fe_2O_3/N-CNTs and α-Fe_2O_3/N-CNTs, suggesting its typical electrical inductance caused by adsorbate-induced relaxations. The similar surplus interfacial process on N-CNTs also creates a barrier for the transfer of electron, and thereby increases its charge transfer resistance value [29]. In sharp contrast, there is almost no apparent resistant characteristic of Nyquist plots of γ-Fe_2O_3/N-CNTs and α-Fe_2O_3/N-CNTs, indicating that both the introduction of γ-Fe_2O_3 and α-Fe_2O_3 to N-CNTs significantly decreased the internal and interfacial resistances of nanocomposites, enhancing the electron-transporting property compared to that of N-CNTs alone.

For better gaining an insight into the electrocatalytic performance of the as-synthesized nanocatalysts during the ORR process, linear sweep voltammetry (LSV) curves were measured using RDE in O_2-saturated 0.1 mol L^{-1} KOH solution at a rotation rate of 1600 rpm. As seen from the Fig. 4c, α-Fe_2O_3/N-CNTs and γ-Fe_2O_3/N-CNTs both had similar onset potential (~ −0.16 V), but more positive than that of N-CNTs and CNTs at −0.21 V. Furthermore, α-Fe_2O_3/N-CNTs possessed higher limiting current density from 2.2 to 3.1 mA cm^{-2} ranging from −0.4 to −0.6 V than that of γ-Fe_2O_3/N-CNTs from 2 to 2.8 mA cm^{-2}, and that of N-CNTs from 1.7 to 1.9 mA cm^{-2}, not to mention CNTs. The obtained results are well in agreement with the experimental observations of CV and further manifest that

the α-Fe_2O_3/N-CNTs held better ORR active sites, more reformative electrolyte diffusion, and higher charge transfer efficiency than γ-Fe_2O_3/N-CNTs. It can be inferred that the α-Fe_2O_3 with appropriate distortions had better opportunity for increasing the charge transfer rate and improving mass adsorption of oxygen atoms on the distortion sites than γ-Fe_2O_3.

RDE voltammetry was further utilized to reveal the kinetic information of the electrocatalytic ORR for γ-Fe_2O_3/N-CNTs and α-Fe_2O_3/N-CNTs. The polarization curves were acquired by scanning the potential from 0 to −0.7 V at a scan rate of 5 mV s^{-1} with different rotation rates in O_2-saturated 0.1 mol L^{-1} KOH solution. As can be seen from Figs 5a and c, the limiting current densities of γ-Fe_2O_3/N-CNTs and α-Fe_2O_3/N-CNTs both increased with the increasing rotation rates ranging from 400 to 2500 rpm. In comparison, α-Fe_2O_3/N-CNTs showed better ORR performances than γ-Fe_2O_3/N-CNTs with a relatively higher current density from −0.3 to −0.7 V. Specifically, a comparable flat and wide current plateau can be observed from α-Fe_2O_3/N-CNTs at −0.3 to −0.55 V, and an evident further increase in limiting diffusion current from −0.55 to −0.7 V compared to γ-Fe_2O_3/N-CNTs. Although the currents of N-CNTs increased with the rotation rates regularly (Fig. S1), it still cannot match the ORR activity of γ-Fe_2O_3/N-CNTs and α-Fe_2O_3/N-CNTs in the limited current density mainly owing to the lack of ORR active site derived from the anchored ferric oxides.

The electron transfer number (n) involved in ORR can be calculated by the corresponding Koutecky-Levich (K-L) plots based on the RDE measurement. The plots at various potentials show good linearity with parallelism over the potential range from −0.45 to −0.65 V, suggesting a similar electron transfer number per O_2 molecule involved and first-order dependence of O_2 kinetics in the ORR. The details of n calculation from K-L equations are given below [30,31]:

$$\frac{1}{J}=\frac{1}{J_K}+\frac{1}{J_L}=\frac{1}{B\omega^{1/2}}+\frac{1}{J_K}, \quad (1)$$

$$B=0.62nFC_0D_0^{2/3}\upsilon^{1/6}, \quad (2)$$

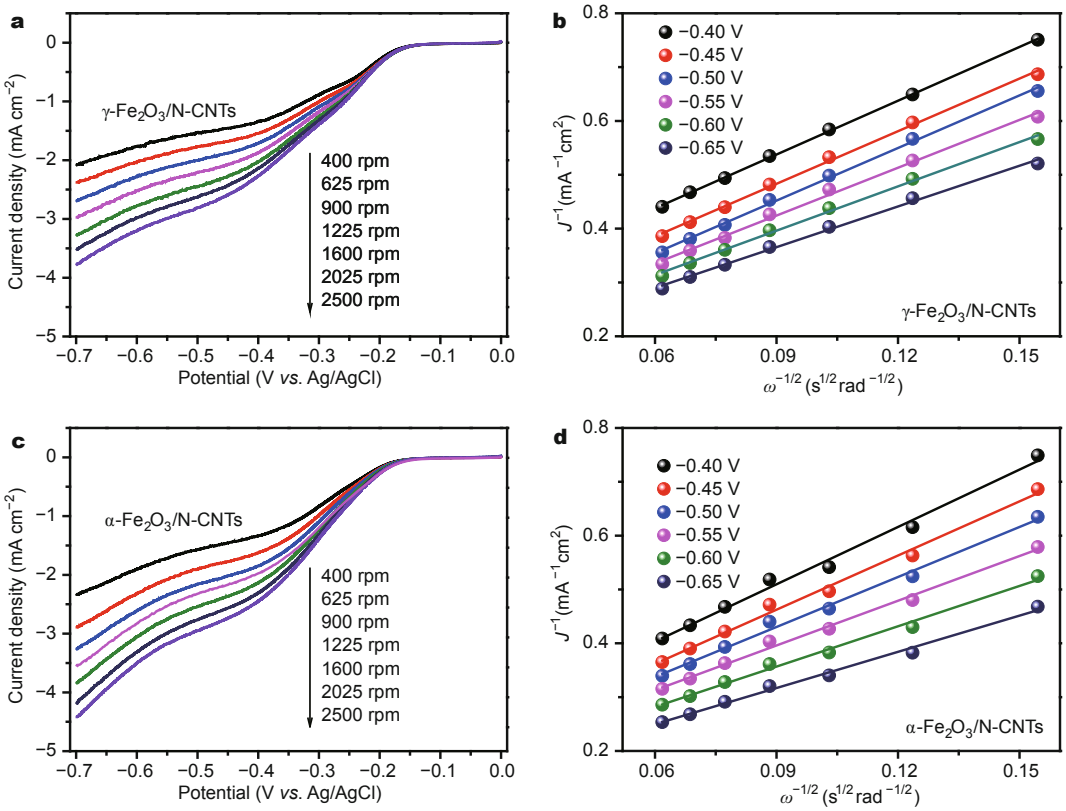

Figure 5 (a and c) RDE curves of the γ-Fe_2O_3/N-CNTs and the α-Fe_2O_3/N-CNTs in O_2-saturated 0.1 mol L^{-1} KOH solution at various rotation rates. Sweep rate: 50 mV s^{-1}. (b and d) The corresponding K-L plots of the γ-Fe_2O_3/N-CNTs and the α-Fe_2O_3/N-CNTs at different potentials.

$$J_K = nFkC_0, \quad (3)$$

where J is the measured current density, J_K and J_L are the kinetic and diffusion limiting current densities, ω is the electrode rotating rate ($\omega = 2pN$, N is the linear rotation speed), n is the overall number of electrons transferred in the oxygen reduction, F is the Faraday's constant (96,485 C mol^{-1}), C_0 is the bulk concentration of O_2, D_0 is the diffusion coefficient of O_2 in the KOH electrolyte, v is the kinematic viscosity of the electrolyte, and k is the electron transfer rate constant.

As shown in Figs 5b and d, according to Equations (1 and 2), the n value of γ-Fe_2O_3/N-CNTs was calculated to be 3.11 at −0.60 V, while the resulting n value was 3.37 for α-Fe_2O_3/N-CNTs. This result illustrates that both the kinetic ORR process via γ-Fe_2O_3/N-CNTs and α-Fe_2O_3/N-CNTs was a combination of two-electron and four-electron reaction pathways. Nevertheless the α-Fe_2O_3/N-CNTs performed more closer to a four-electron ORR pathway that reduced O_2 directly to OH^- in alkaline oxygen reduction compared with γ-Fe_2O_3/N-CNTs, indicating that the structured N-CNTs with α-Fe_2O_3 nanoparticles exhibited abundant oxygen reduction active reaction sites. It can be inferred that except for the nitrogen doping site can serve as catalytic center for ORR, α-Fe_2O_3 further provided more ORR "hotspot" than γ-Fe_2O_3. In addition, the average n value of N-CNTs calculated from the diffusion potential ranges (−0.4 to −0.6 V) was 2.66 (inset in Fig. S1), demonstrating that it possessed weaker catalytic activity for ORR than γ-Fe_2O_3/N-CNTs and α-Fe_2O_3/N-CNTs, not to mention the commercial Pt/C (n = 3.89, see Fig. S2). From the above results, it is suggested that the introduction of α-Fe_2O_3 and γ-Fe_2O_3 to N-CNTs could enhance the catalytic performance towards oxygen with abundant exposed active sites. The simultaneous pyrolysis of Fe_2O_3 and nitrogen doping procedure endowed the nanocatalysts not only with pyridinic- and quaternary-N for stimulating ORR, but also with the specific crystal type of Fe_2O_3 as added active ORR sites.

The electrocatalytic performance in the resistance of methanol crossover and long-term stability are of great importance for the promising industrial application in fuel cells. In Fig. 6a, a clear positive jump in the Pt/C system appeared when 3 mol L^{-1} methanol was added at around 300 s. While the γ-Fe_2O_3/N-CNTs and α-Fe_2O_3/N-CNTs both retained stable current response as methanol was introduced, suggesting that they were promising candidates particularly for direct methanol fuel cell. The electrocatalytic durabilities of γ-Fe_2O_3/N-CNTs and α-Fe_2O_3/N-CNTs were also evaluated. As shown in Fig. 6b, the γ-Fe_2O_3/N-CNTs and α-Fe_2O_3/N-CNTs maintained 89.1% and 84.7% of the original activity within 35,000 s, while the relative current of commercial Pt/C decreased gradually to 56.9%. The results demonstrate that the synthesized γ-Fe_2O_3/N-CNTs and α-Fe_2O_3/N-CNTs are good at chemical stability and have potential use in direct methanol and alkaline fuel cells compared to Pt/C.

CONCLUSIONS

The well-defined γ-Fe_2O_3 nanotubes and α-Fe_2O_3 nanospheres supported on N-CNTs nanocatalysts were successfully synthesized through a cooperative process of crystal formation and heteroatom nitrogen doping. The differences of electrocatalytic performance for ORR between γ-Fe_2O_3/N-CNTs and α-Fe_2O_3/N-CNTs were investigated carefully. The results show that α-Fe_2O_3/N-CNTs were more capable for oxygen reduction with more active response of peak potential and current compared to that of γ-Fe_2O_3/N-CNTs. Moreover, it also held highly efficient and preferable four-electron transfer of ORR kinetic process. The formation of α-Fe_2O_3 with the right amount of

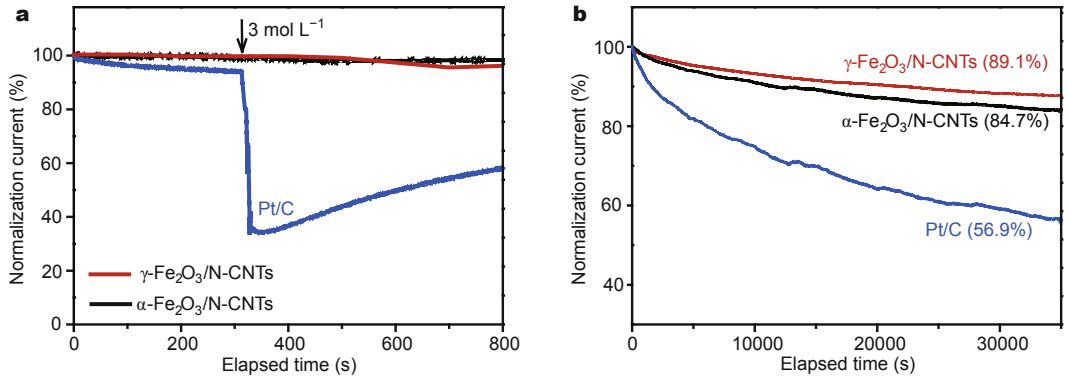

Figure 6 The current-time (I-t) responses of the γ-Fe_2O_3/N-CNTs, α-Fe_2O_3/N-CNTs and Pt/C at −0.2 V in O_2-saturated 0.1 mol L^{-1} KOH solution with a rotation rate of 1600 rpm: (a) with the addition of 3 mol L^{-1} methanol at around 300 s; (b) with a long elapsed time of 35,000 s.

distortions not only provided more ORR active sites than that of γ-Fe_2O_3, but also decreased the difficulty of nitrogen doping on CNTs, resulting in more N doped active sites for ORR. Both the γ-Fe_2O_3/N-CNTs and α-Fe_2O_3/N-CNTs show excellent catalytic stability and methanol resistance, which make them ideal candidates of non-noble ORR catalysts for fuel cells application.

Received 1 September 2015; accepted 14 September 2015; published online 18 September 2015

1 Yang Z, Zhou X, Nie H, Yao Z, Huang S. Facile construction of manganese oxide doped carbon nanotube catalysts with high activity for oxygen reduction reaction and investigations into the origin of their activity enhancement. ACS Appl Mater Interfaces, 2011, 3: 2601–2606
2 Dai L, Xue Y, Qu L, Choi HJ, Baek JB. Metal-free catalysts for oxygen reduction reaction. Chem Rev, 2015, 115: 4823–4892
3 Sun M, Liu H, Liu Y, Qu J, Li J. Graphene-based transition metal oxide nanocomposites for the oxygen reduction reaction. Nanoscale, 2015, 7: 1250–1269
4 Liu M, Zhang R, Chen W. Graphene-supported nanoelectrocatalysts for fuel cells: synthesis, properties, and applications. Chem Rev, 2014, 114: 5117–5160
5 Qian F, Wang H, Ling Y, *et al*. Photoenhanced electrochemical interaction between shewanella and a hematite nanowire photoanode. Nano Letters, 2014, 14: 3688–3693
6 Sun Z, Yuan H, Liu Z, Han B, Zhang X. A highly efficient chemical sensor material for H_2S: α-Fe_2O_3 nanotubes fabricated using carbon nanotube templates. Adv Mater, 2005, 17: 2993–2997
7 Kay A, Cesar I, Grätzel M. New benchmark for water photooxidation by nanostructured α-Fe_2O_3 films. J Am Chem Soc, 2006, 128: 15714–15721
8 Sun M, Dong Y, Zhang G, Qu J, Li J. α-Fe_2O_3 spherical nanocrystals supported on CNTs as efficient non-noble electrocatalysts for the oxygen reduction reaction. J Mater Chem A, 2014, 2: 13635–13640
9 Zhou W, Lin L, Wang W, *et al*. Hierarchial mesoporous hematite with "electron-transport channels" and its improved performances in photocatalysis and lithium ion batteries. J Phys Chem C, 2011, 115: 7126–7133
10 Wu C, Yin P, Zhu X, OuYang C, Xie Y. Synthesis of hematite (α-Fe_2O_3) nanorods: diameter-size and shape effects on their applications in magnetism, lithium ion battery, and gas sensors. J Phys Chem B, 2006, 110: 17806–17812
11 Yun H, Liu X, Paik T, *et al*. Size- and composition-dependent radio frequency magnetic permeability of iron oxide nanocrystals. ACS Nano, 2014, 8: 12323–12337
12 Zhao N, Ma W, Cui Z, *et al*. Polyhedral maghemite nanocrystals prepared by a flame synthetic method: preparations, characterizations, and catalytic properties. ACS Nano, 2009, 3: 1775–1780
13 Li N, Li K, Wang S, *et al*. Gold embedded maghemite hybrid nanowires and their gas sensing properties. ACS Appl Mater Interfaces, 2015, 7: 10534–10540
14 Wu Y, Zhu P, Reddy M, Chowdari B, Ramakrishna S. Maghemite nanoparticles on electrospun CNFs template as prospective lithium-ion battery anode. ACS Appl Mater Interfaces, 2014, 6: 1951–1958
15 Morin G, Ona-Nguema G, Wang Y, *et al*. Extended X-ray absorption fine structure analysis of arsenite and arsenate adsorption on maghemite. Environ Sci Technol, 2008, 42: 2361–2366
16 Wen Z, Li J. Hierarchically structured carbon nanocomposites as electrode materials for electrochemical energy storage, conversion and biosensor systems. J Mater Chem, 2009, 19: 8707–8713
17 Chen R, Yan J, Liu Y, Li J. Three-dimensional nitrogen-doped graphene/MnO nanoparticle hybrids as a high-performance catalyst for oxygen reduction reaction. J Phys Chem C, 2015, 119: 8032–8037
18 Jing L, Qu Y, Su H, Yao C, Fu H. Synthesis of high-activity TiO_2-based photocatalysts by compounding a small amount of porous nanosized $LaFeO_3$ and the activity-enhanced mechanisms. J Phys Chem C, 2011, 115: 12375–12380
19 Dong Y, Wu Y, Liu M, Li J. Electrocatalysis on shape-controlled titanium nitride nanocrystals for the oxygen reduction reaction. ChemSusChem, 2013, 6: 2016–2021
20 Dong J, Qu X, Wang L, Wang T. Electrochemical behavior of nitrogen-doped carbon nanotube modified electrodes. Acta Chim Sinica, 2007, 21: 2405–2410
21 Rao C, Cabrera C, Ishikawa Y. In search of the active site in nitrogen-doped carbon nanotube electrodes for the oxygen reduction reaction. J Phys Chem Lett, 2010, 1: 2622–2627
22 Eder D. Carbon nanotube-inorganic hybrids. Chem Rev, 2010, 110: 1348–1385
23 Kim D, Li O, Saito N. Enhancement of ORR catalytic activity by multiple heteroatom-doped carbon materials. Phys Chem Chem Phys, 2015, 17: 407–413
24 Chen W, Pan X, Bao X. Tuning of redox properties of iron and iron oxides via encapsulation within carbon nanotubes. J Am Chem Soc, 2007, 129: 7421–7426
25 Wang L, Yin J, Zhao L, *et al*. Ion-exchanged route synthesis of Fe_2N-N-doped graphitic nanocarbons composite as advanced oxygen reduction electrocatalyst. Chem Commun, 2013, 49: 3022–3024
26 Chung H, Won J, Zelenay P. Active and stable carbon nanotube/nanoparticle composite electrocatalyst for oxygen reduction. Nat Commun, 2013, 4: 1922–1927
27 Ci S, Cai P, Wen Z, Li J. Graphene-based electrode materials for microbial fuel cells. Sci China Mater, 2015, 58: 496–509
28 Wang Y, Shao Y, Matson D, Li J, Lin Y. Nitrogen-doped graphene and its application in electrochemical biosensing. ACS Nano, 2010, 4: 1790–1798
29 Zabet-Khosousi A, Dhirani A. Charge transport in nanoparticle assemblies. Chem Rev, 2008, 108: 4072–4124
30 Xing T, Zheng Y, Li L, *et al*. Observation of active sites for oxygen reduction reaction on nitrogen-doped multilayer graphene. ACS Nano, 2014, 8: 6856–6862
31 Silva R, Voiry D, Chhowalla M, Asefa T. Efficient metal-free electrocatalysts for oxygen reduction: polyaniline-derived N- and O-doped mesoporous carbons. J Am Chem Soc, 2013, 135: 7823–7826

Acknowledgements This work was supported by the Major Program of National Natural Science Foundation of China (51290282), the National Science Fund for Distinguished Young Scholars of China (51225805), the National Natural Science Foundation of China (51572139), and the National Basic Research Program of China (2013CB934004).

Author contributions Li J and Sun M designed the experiments; Sun M and Zhang G performed the experiments and the characterization. Liu H and Liu Y helped with the sample characterization. Sun M and Li J wrote the paper. All the authors contributed to the general discussion.

Conflict of interest The authors declare that they have no conflict of interest.

Supplementary information Supporting data are available in the online version of the paper.

Jinghong Li is currently a Cheung Kong Professor at the Department of Chemistry at Tsinghua University, China. He received his BSc degree from the University of Science and Technology of China in 1991, and PhD degree from Changchun Institute of Applied Chemistry, Chinese Academy of Sciences in 1996. He spent several years at the University of Illinois at Urbana-Champaign, University of California at Santa Barbara, Clemson University, and Evonyx Inc., New York. He returned to Changchun in May 2001 and then joined the faculty of Tsinghua University in July 2004. His current research interests include electroanalytical chemistry, bio-electrochemistry and sensors, physical electrochemistry and interfacial electrochemistry, electrochemical materials science and nanoscopic electrochemistry, fundamental aspects of energy conversion and storage, advanced battery materials, and photoelectrochemistry. He has published over 290 papers in international, peer-reviewed journals with more than 18,000 citations and h-index of 72.

中文摘要 本论文采用空气煅烧与氮气/氨气退火两步法制备了α-Fe_2O_3/N-CNTs和γ-Fe_2O_3/N-CNTs高效氧气还原反应催化剂. X射线衍射与X射线光电子能谱等结果显示: 球状的α-Fe_2O_3与立方体状的γ-Fe_2O_3较好地分散在氮掺杂的碳纳米管上; 不同的退火温度造成γ-Fe_2O_3/N-CNTs中氮的掺杂量约为1.06%, 而α-Fe_2O_3/N-CNTs中氮掺杂量约为1.94%. 从拉曼光谱结果发现, α-Fe_2O_3/N-CNTs的I_D/I_G值(1.26)大于γ-Fe_2O_3/N-CNTs的I_D/I_G值(1.18), 说明α-Fe_2O_3/N-CNTs表面可因较大的碳缺陷程度而产生更多的氧还原活性电位. 电化学性能表征结果再次印证: 相比较于γ-Fe_2O_3/N-CNTs, N-CNTs和CNTs, α-Fe_2O_3/N-CNTs具有更低的氧还原起始电位(−0.21 V)和峰值电位(−0.27 V). 在碱性条件下, 氧气在α-Fe_2O_3/N-CNTs表面更易发生接近4电子的还原反应. 另外, 与Pt/C相比, α-Fe_2O_3/N-CNTs和γ-Fe_2O_3/N-CNTs皆具有较好的催化耐久性与稳定性, 进一步显示了二者在清洁能源电池领域的应用价值与潜力.